An updated-Lagrangian damage mechanics formulation for modeling the creeping flow and fracture of ice sheets

Supplementary Material

Stephen Jiménez[a], Ravindra Duddu[a,*], Jeremy Bassis[b]

[a]*Department of Civil and Environmental Engineering, Vanderbilt Univeristy, Nashville, TN.*
[b]*Department of Atmospheric, Oceanic, and Space Sciences, University of Michigan, Ann Arbor, MI.*

Abstract

This document contains supplementary material for the article entitled, "An updated-Lagrangian damage mechanics formulation for modeling the creeping flow and fracture of ice sheets." The document is divided into three parts. In Section 1 we summarize the total Lagrangian Maxwell viscoelastic formulation [1] which is implemented in the benchmark studies in Sections 4.2 and 4.3 of the main article. In Section 2, we present a stabilized P1-P1 element formulation [2–4] and an enriched MINI-element using bubble functions as stable alternatives to the P3-P1 element, and then show comparative studies. Finally, in Section 3 we present the Newton's method for solving the nonlinear Stokes equations. All simulations are conducted using FEniCS open-source finite element software (http://fenicsproject.org/).

1. Small-deformation Maxwell viscoelasticity

1.1. Constitutive law

Here we review the salients features of the small-deformation Maxwell viscoelastic model based on a total Lagrangian approach for simulating creep damage evolution in ice [5]. Considering that polycrystalline ice behaves isotropically and assuming small deformations, the total strain ε^{t} and total strain rate $\dot{\varepsilon}^{\mathrm{t}}_{ij}$ can be additively decomposed into its elastic and viscous components as

$$\varepsilon^{\mathrm{t}}_{ij} = \varepsilon^{\mathrm{e}}_{ij} + \varepsilon^{\mathrm{v}}_{ij}; \quad \dot{\varepsilon}^{\mathrm{t}}_{ij} = \dot{\varepsilon}^{\mathrm{e}}_{ij} + \dot{\varepsilon}^{\mathrm{v}}_{ij}, \tag{1}$$

*Corresponding author
Email address: ravindra.duddu@vanderbilt.edu (Ravindra Duddu)

where the subscript indices denote tensor components. The elastic stress-strain relationship in the effective space and physical space are given by

$$\widetilde{\sigma}_{ij} = C_{ijkl}\varepsilon^{\mathrm{e}}_{kl}; \quad \sigma_{ij} = C^{\mathrm{dam}}_{ijkl}\varepsilon^{\mathrm{e}}_{kl}, \tag{2}$$

where σ_{ij} is the Cauchy stress tensor, C_{ijkl} is the fourth-order stiffness tensor, and $C^{\mathrm{dam}}_{ijkl} = (1-D)C_{ijkl}$. For linear elasticity, the components of C_{ijkl} are

$$C_{ijkl} = \frac{E_Y}{3\,(1-2\nu)}\delta_{ij}\delta_{kl} + \frac{E_Y}{2\,(1+\nu)}\left(\delta_{ik}\delta_{jl} + \delta_{il}\delta_{jk} - \frac{2}{3}\delta_{ij}\delta_{lk}\right), \tag{3}$$

where $E_Y = 9500$ MPa and $\nu = 0.35$ are the Young's modulus and Poisson's ratio of ice, respectively, and δ_{ij} is Kronecker's delta.

The viscous strain rate $\dot{\varepsilon}^{\mathrm{v}}$ is given by the power law [6, 7]

$$\dot{\varepsilon}^{\mathrm{v}}_{ij} = \frac{3}{2}K_N\left(\frac{3}{2}\widetilde{\tau}_{kl}\widetilde{\tau}_{kl}\right)^{(N-1)/2}\widetilde{\tau}_{ij}, \tag{4}$$

where the coefficient $K_N = 1.588 \times 10^{-7}$ MPa^{-3} s^{-1} at $T = -10^{\circ}C$ and exponent $N = 3$ are viscous parameters, and $\widetilde{\tau}_{ij}$ is the effective deviatoric stress. Note the similarity to Equation (17) from the main article, which is based on the Glen's flow law [8] and repeated below:

$$\dot{\epsilon}_{ij} = A\,(\widetilde{\tau}^{\mathrm{eq}})^{N-1}\,\widetilde{\tau}_{ij} \tag{5}$$

For the exponent $N = 3$, a relationship between K_N and A can be established by equating $\dot{\varepsilon}^{\mathrm{v}}_{ij}$ and $\dot{\epsilon}_{ij}$

$$\frac{3}{2}K_N\left(\frac{3}{2}\widetilde{\tau}_{kl}\widetilde{\tau}_{kl}\right)\widetilde{\tau}_{ij} = A(\widetilde{\tau}^{\mathrm{eq}})^2\widetilde{\tau}_{ij}. \tag{6}$$

By removing the $\widetilde{\tau}_{ij}$ term from each side of the equation and then substituting the relation $(\widetilde{\tau}^{\mathrm{eq}})^2 = \frac{1}{2}\widetilde{\tau}_{kl}\widetilde{\tau}_{kl}$, it follows that $\frac{9}{2}K_N = A$. In this study, we select an experimentally calibrated value for A used in the Stokes model and then calculate K_N for the Maxwell viscoelastic model.

1.2. Maxwell viscoelastic model in deviatoric space

In this section, we show that the small-deformation viscoelastic model behaves like a Maxwell model in deviatoric space. Let us additively decompose the strain into volumetric (denoted with superscript vol) and deviatoric (superscript dev) components

$$\varepsilon^{\mathrm{t\ vol}}_{ij} = \frac{1}{3}\varepsilon^{\mathrm{t}}_{kk}\delta_{ij}, \quad \varepsilon^{\mathrm{t\ dev}}_{ij} = \varepsilon^{\mathrm{t}}_{ij} - \varepsilon^{\mathrm{t\ vol}}_{ij}, \tag{7}$$

with $\varepsilon_{ij}^{\mathrm{e}}$ and $\varepsilon_{ij}^{\mathrm{v}}$ similarly split into volumetric and deviatoric parts. The additive decomposition of strain in Equation (1) still holds in the volumetric and deviatoric spaces such that $\varepsilon_{ij}^{\mathrm{t}\,\mathrm{vol}} = \varepsilon_{ij}^{\mathrm{e}\,\mathrm{vol}} + \varepsilon_{ij}^{\mathrm{v}\,\mathrm{vol}}$ and $\varepsilon_{ij}^{\mathrm{t}\,\mathrm{dev}} = \varepsilon_{ij}^{\mathrm{e}\,\mathrm{dev}} + \varepsilon_{ij}^{\mathrm{v}\,\mathrm{dev}}$. Then, the effective Cauchy stress and deviatoric stress can be represented in terms of $\varepsilon_{ij}^{\mathrm{e}\,\mathrm{vol}}$ and $\varepsilon_{ij}^{\mathrm{e}\,\mathrm{dev}}$ as

$$\widetilde{\sigma}_{ij} = \frac{E_Y}{(1-2\nu)}\left(\varepsilon_{ij}^{\mathrm{e}\,\mathrm{vol}}\right) + \frac{E_Y}{(1+\nu)}\left(\varepsilon_{ij}^{\mathrm{e}\,\mathrm{dev}}\right), \quad \widetilde{\tau}_{ij} = \frac{E_Y}{(1+\nu)}\left(\varepsilon_{ij}^{\mathrm{e}\,\mathrm{dev}}\right). \tag{8}$$

Since the viscous strain rate $\dot{\varepsilon}_{ij}^{\mathrm{v}}$ of ice is driven purely by deviatoric stresses (Eq. 4), the volumetric component $\dot{\varepsilon}_{ij}^{\mathrm{v}\,\mathrm{vol}} = 0$, thus leaving $\dot{\varepsilon}_{ij}^{\mathrm{v}} = \dot{\varepsilon}_{ij}^{\mathrm{v}\,\mathrm{dev}}$. For the deviatoric component of total strain rate $\dot{\varepsilon}_{ij}^{\mathrm{t}\,\mathrm{dev}}$ we now have

$$\begin{aligned} \dot{\varepsilon}_{ij}^{\mathrm{t}\,\mathrm{dev}} &= \dot{\varepsilon}_{ij}^{\mathrm{e}\,\mathrm{dev}} + \dot{\varepsilon}_{ij}^{\mathrm{v}\,\mathrm{dev}} \\ &= \left[\frac{(1+\nu)}{E_Y}\right]\dot{\widetilde{\tau}}_{ij} + \left[\frac{3}{2}K_N\left(\frac{3}{2}\widetilde{\tau}_{kl}\widetilde{\tau}_{kl}\right)^{(N-1)/2}\right]\widetilde{\tau}_{ij}, \end{aligned} \tag{9}$$

which matches the form of the 1D Maxwell viscoelastic model

$$\dot{\varepsilon} = \frac{\dot{\sigma}}{\hat{E}_Y} + \frac{\sigma}{\hat{\eta}}, \tag{10}$$

where $\hat{\eta}$ is a viscosity parameter and $\hat{E}_Y$ is an elastic modulus parameter. The $1/2\mu$ term is analagous to the elastic coefficient $1/\hat{E}$, and $\left[\frac{3}{2}K_N\left(\frac{3}{2}\widetilde{\tau}_{kl}\widetilde{\tau}_{kl}\right)^{(N-1)/2}\right]$ is analagous to the viscosity coefficient $1/\hat{\eta}$.

1.3. Total Lagrangian implementation

We select a total Lagrangian frame of reference to describe motion in the viscoelastic model. Motion is characterized by a displacement field $\boldsymbol{u}\left({}^0\boldsymbol{x}, t\right) = u_i\hat{\boldsymbol{e}}_i$ representing the positions of points relative to the initial reference configuration ${}^0\Omega$ with coordinates ${}^0\boldsymbol{x} = {}^0x_i\hat{\boldsymbol{e}}_i$. The kinematic strain-displacement relation is taken by assuming small deformations

$$\varepsilon_{ij}^{\mathrm{t}} = \frac{1}{2}\left(\frac{\partial\, u_i}{\partial\, {}^0x_j} + \frac{\partial\, u_j}{\partial\, {}^0x_i}\right). \tag{11}$$

The strong form of the viscoelastic equation is written with respect to reference coordinates The equilibrium equation of the viscoelasticity model is taken as a force balance describing the time-dependent deformation of solids in response to applied loads. The solution of the equilibrium equation is a displacement field

$\boldsymbol{u}(\boldsymbol{X}, t)$ representing the positions of points relative to some reference configuration with coordinates $\boldsymbol{X}$, and thus describes motion through a Lagrangian frame of reference. In indicial form, the equilibrium equation is written as,

$$\frac{\partial\, \sigma_{ij}}{\partial\, {}^0x_j} + b_i = 0 \qquad \text{on } {}^0\Omega, \tag{12}$$

with Dirichlet and Neumann boundary conditions

$$\begin{aligned} u_i &= \bar{u}_i \quad \text{on } {}^0\Gamma^{\mathrm{D}}, \\ \sigma_{ij}\hat{n}_j &= \bar{\mathcal{T}}_i \quad \text{on } {}^0\Gamma^{\mathrm{N}}, \end{aligned} \tag{13}$$

where σ_{ij} and b_i are components of the Cauchy stress tensor and external body force vector, respectively; $\bar{\boldsymbol{u}}$ is a Dirichlet boundary condition (i.e., applied displacement); $\hat{\boldsymbol{n}}$ is an outward normal unit vector along the boundary; and $\bar{\boldsymbol{\mathcal{T}}}$ is a vector of applied tractions. The full details of the finite element implementation of this total Lagrangian formulation can be found in [5].

2. Lower-order alternatives to mixed finite elements

It is well known that solving the Stokes equations with equal-order interpolation of velocity and pressure does not satisfy the Ladyzhenskaya–Babuška–Brezzi (LBB) stability condition, thus leading to "checkerboard" oscillations in the pressure solution. To avoid this, a mixed-order finite element is typically employed which uses quadratic (P2) or cubic (P3) interpolation for the velocity field, while using a linear (P1) interpolation for pressure. Increasing the order of interpolation can significantly increase the computational expense, however, especially for large-scale simulations and 3D problems. Thus, several stabilized lower-order methods have been proposed, namely, the stabilized P1-P1 [2–4] and the MINI-element [9].

2.1. Stabilized P1-P1 element

The stabilized P1-P1 element assumes equal-order (linear) interpolation for velocity and pressure and satisfies the LBB condition by introducing a stabilization term (highlighted with blue text) to the variational form. Following [2, 3], we write the weak form as,

Find ${}^{n+1}\boldsymbol{v} \in \mathcal{V}$ and ${}^{n+1}\widetilde{p} \in \mathcal{S}$ such that $\forall\ \boldsymbol{w} \in \mathcal{V}$ and $q \in \mathcal{S}$:

$$\left.\begin{aligned}
&\int_{{}^{n}\Omega} \frac{\partial\, w_i}{\partial\, {}^{n}x_j} \left\{ [1 - {}^{n}D]\, \eta\left({}^{n+1}\boldsymbol{v}\right) \left[\frac{\partial\, {}^{n+1}v_i}{\partial\, {}^{n}x_j} + \frac{\partial\, {}^{n+1}v_j}{\partial\, {}^{n}x_i} \right] \right\} \mathrm{d}\Omega \\
&- \int_{{}^{n}\Omega} [1 - {}^{n}D] \frac{\partial\, w_i}{\partial\, {}^{n}x_i}\, {}^{n+1}\widetilde{p}\, \mathrm{d}\Omega + \zeta h^2 \int_{{}^{n}\Omega} \left(\frac{\partial\, q}{\partial\, {}^{n}x_j} \frac{\partial\, p}{\partial\, {}^{n}x_j} \right) \mathrm{d}\Omega \\
&- \int_{{}^{n}\Omega} \psi\left({}^{n}D\right) w_i\, {}^{n}b_i\, \mathrm{d}\Omega - \zeta h^2 \int_{{}^{n}\Omega} \left(\frac{\partial\, q}{\partial\, {}^{n}x_j} \psi\left({}^{n}D\right) {}^{n}b_j \right) \mathrm{d}\Omega \\
&\qquad\qquad \int_{{}^{n}\Gamma^{\mathrm{N}}} w_i\, {}^{n}\overline{T}_i\, \mathrm{d}\Gamma = 0 \\
&\qquad\qquad\qquad\qquad \int_{{}^{n}\Omega} \psi\left({}^{n}D\right) q \frac{\partial\, {}^{n+1}v_i}{\partial\, {}^{n}x_i}\, \mathrm{d}\Omega = 0
\end{aligned}\right\} \quad \text{on } {}^{n}\Omega, \tag{14}$$

where h is the element size and $\zeta = 2 \times 10^{-10}$ is a chosen stabilization parameter. The first stabilization term in Equation (14) essentially is the $\varepsilon\left(\nabla q, \nabla p\right)$ term in [10] circumvents the LBB condition, and the second stabilization term makes the formulation mathematically consistent [11]. However, the drawback of this particular stabilized formulation is that the choice of ζ is typically made in an *ad hoc* manner [12]. While the stabilized P1-P1 element alleviates the checkerboard oscillations in pressure, we found that the incompressibility condition is still not well enforced. This can lead to deviatoric stresses inconsistent with those predicted by P3-P1 or P2-P1 elements, thus changing the Hayhurst stress around the notch tip and causing different rates of crevasse growth, as shown in Sections 4.2.2 and 4.3.2 in the main article.

2.2. MINI-element

Another stable alternative to mixed-order elements is the enriched MINI-element [9]. The MINI-element assumes linear velocity interpolants enriched using a bubble function, and thus has fewer degrees of freedom than a mixed-order finite element. A caveat is that triangular (T3) and tetrahedral (T4) MINI-elements alleviate oscillations in pressure, but quadrilateral (Q4) and hexahedral (Q8) MINI-elements can suffer from instability, according to Turner et al. [12]. Herein, we compare the performance of MINI-elements to P3-P1, P2-P1, and stabilized P1-P1 elements by simulating crack growth under gravity-driven creep flow for 3 months. The performance of the MINI-element is evaluated by plotting the predicted crevasse depth versus time, which is the most important result from a ice sheet stability perspective. The direct enforcement of

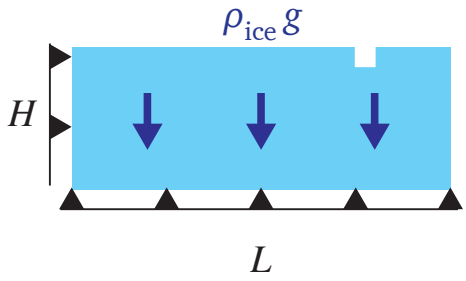

Figure 1: Domain setup with gravitational body force $\rho_{\text{ice}} g$ and a 10 m $\times$ 10 m notch placed along the top surface of the slab, where $H = 125$ m and $L = 500$ m. The notch is centered at the "three-quarter" mark, that is, 375 m from the left edge of the slab.

the free-slip Dirichlet boundary condition is difficult in FEniCS software, and so we implement no-slip boundary conditions along the the left and bottom boundaries instead; however, we note that weak formulations using penalty or Nitsche's method can be used to implement free slip conditions, which will be considered in future studies. The purpose of this study is to simply check the viability of the MINI-element for simulating crevasse propagation. All simulations are performed on a rectangular slab of ice that is 500 m $\times$ 125 m (length L $\times$ height H), as shown in Figure 1. A 10 m $\times$ 10 m notch is centered at the three-quarter mark along the slab, that is, 375 m from the left edge.

The results of this study are shown in Figure 2 wherein we plot the normalized crevasse depth d versus time t. In Table 1, we also list the crack tip damage initiation times and final normalized crevasse depth for each element type considered. The different elements predict very similar crack tip damage initiation times (i.e., around 9 days) and similar crack growth rates following damage initiation; however the P3-P1 and P2-P1 elements ultimately predict deeper crack penetration than the MINI- and stabilized P1-P1 elements. Although the MINI- and stabilized P1-P1 elements slightly under-predict the final crevasse depth, the simulations ran more than four times faster than the simulation using P3-P1 elements on the same mesh (i.e., the same number of triangular cells). We conclude from this study that the MINI-element is a stable alternative to the P3-P1 element; however, the stabilized P1-P1 element is easier to implement in FEniCS software and runs slightly faster than the MINI-element due to fewer degrees of freedom. The stabilized P1-P1 element also agrees slightly better with the P3-P1 and P2-P1 elements in terms of crack tip damage initiation time and final crevasse depth. Further, developments in stabilized methods is required to

Table 1: Crack tip damage initiation time (in days) and final normalized crevasse depth d after 90 days for the gravity-driven flow problem with no-slip boundary conditions.

Element	Damage Initiation	Final Depth
MINI	8.26 days	46.6%
Stab. P1-P1	9.25 days	48.2%
P2-P1	9.21 days	51.3%
P3-P1	8.88 days	52.8%

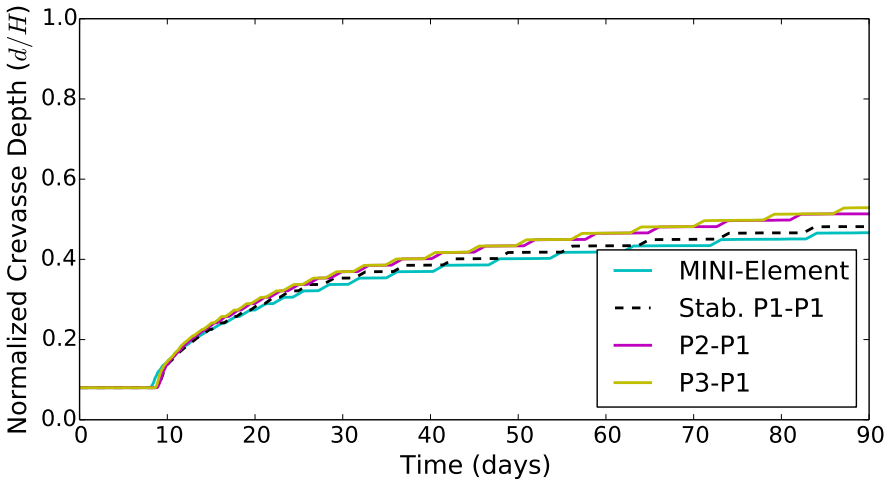

Figure 2: Crevasse depth (d) normalized with the domain height ($H = 125$ m) plotted as a function of time over 90 days for different finite element types.

address the discrepancies in damage evolution in nonlinear viscous media.

3. Newton's method

The Newton's method is an alternative scheme to the Picard (fixed point) iterations presented Algorithm 2 in the main article for solving the nonlinear Stokes equations [13]. Whereas the Picard iteration scheme linearizes the PDE by making the nonlinear viscosity a function of velocity ${}^{n+1}_{(m)}\boldsymbol{v}$ from the previous iteration, the Newton's method linearizes the PDE by introducing velocity and pressure increments and linearizing the viscosity using a Taylor expansion,

$$\eta\left({}^{n+1}_{(m+1)}\boldsymbol{v}\right) = \eta\left({}^{n+1}_{(m)}\boldsymbol{v}\right) + \frac{\partial\eta}{\partial\,{}^{n+1}_{(m)}\boldsymbol{v}} \cdot {}^{n+1}\delta\boldsymbol{v}, \tag{15}$$

where ${}^{n+1}\delta\boldsymbol{v}$ is the velocity increment and ${}^{n+1}\delta\widetilde{p}$ is the pressure increment defined as

$$\begin{aligned} {}^{n+1}\delta\boldsymbol{v} &= {}^{n+1}_{(m+1)}\boldsymbol{v} - {}^{n+1}_{(m)}\boldsymbol{v}, \\ {}^{n+1}\delta\widetilde{p} &= {}^{n+1}_{(m+1)}\widetilde{p} - {}^{n+1}_{(m)}\widetilde{p}, \end{aligned} \tag{16}$$

between Newton iterations m and $m+1$. The derivative term in Equation (15) can be evaluated by applying the chain rule,

$$\begin{aligned} \frac{\partial \eta}{\partial\, {}^{n+1}_{(m)}\boldsymbol{v}} \cdot {}^{n+1}\delta\boldsymbol{v} &= \frac{\partial \eta}{\partial \mathcal{D}_{\mathrm{II}}\left({}^{n+1}_{(m)}\boldsymbol{v}\right)} \frac{\partial \mathcal{D}_{\mathrm{II}}\left({}^{n+1}_{(m)}\boldsymbol{v}\right)}{\partial \mathcal{D}\left({}^{n+1}_{(m)}\boldsymbol{v}\right)} : \frac{\partial \mathcal{D}\left({}^{n+1}_{(m)}\boldsymbol{v}\right)}{\partial\, {}^{n+1}_{(m)}\boldsymbol{v}} \cdot {}^{n+1}\delta\boldsymbol{v} \\ &= \frac{\partial \eta}{\partial \mathcal{D}_{\mathrm{II}}\left({}^{n+1}_{(m)}\boldsymbol{v}\right)} \mathcal{D}\left({}^{n+1}_{(m)}\boldsymbol{v}\right) : \mathcal{D}\left({}^{n+1}\delta\boldsymbol{v}\right), \end{aligned} \tag{17}$$

where the term $\mathcal{D}(\cdot)$ is the symmetric gradient operator,

$$\mathcal{D}(\boldsymbol{v}) = \frac{1}{2}\left(\nabla\boldsymbol{v} + \nabla\boldsymbol{v}^{\top}\right), \tag{18}$$

which yields the strain rate tensor when operating on velocity. Because $\mathcal{D}(\cdot)$ is a linear operator, it follows that

$$\mathcal{D}\left({}^{n+1}\delta\boldsymbol{v}\right) = \mathcal{D}\left({}^{n+1}_{(m+1)}\boldsymbol{v}\right) - \mathcal{D}\left({}^{n+1}_{(m)}\boldsymbol{v}\right). \tag{19}$$

The term $\mathcal{D}_{\mathrm{II}}(\cdot)$ is the second strain rate invariant given by

$$\mathcal{D}_{\mathrm{II}}(\boldsymbol{v}) = \frac{1}{2}\mathcal{D}(\boldsymbol{v}) : \mathcal{D}(\boldsymbol{v}), \tag{20}$$

such that $\dot{\epsilon}^{\mathrm{eq}} = \sqrt{\mathcal{D}_{\mathrm{II}}(\boldsymbol{v})}$. The nonlinear viscosity $\eta(\boldsymbol{v}) = \frac{1}{2}B\left[\mathcal{D}_{\mathrm{II}}(\boldsymbol{v}) + \gamma\right]^{-1/3}$ with regularization parameter $\gamma = 10^{-14}$. Thus, the derivative of η with respect to $\mathcal{D}_{\mathrm{II}}$ is taken as

$$\frac{\partial \eta}{\partial \mathcal{D}_{\mathrm{II}}\left({}^{n+1}_{(m)}\boldsymbol{v}\right)} = -\frac{1}{3}\left[\frac{\eta\left({}^{n+1}_{(m)}\boldsymbol{v}\right)}{\mathcal{D}_{\mathrm{II}}\left({}^{n+1}_{(m)}\boldsymbol{v}\right) + \gamma}\right]. \tag{21}$$

Let us now write the weak form of the nonlinear Stokes equations on the current reference configuration ${}^{n}\Omega$ in tensorial notation at particular iteration $m+1$:

Find ${}^{n+1}\delta\boldsymbol{v} \in \mathcal{V}$ and ${}^{n+1}\delta\widetilde{p} \in \mathcal{S}$ such that $\forall\ \boldsymbol{w} \in \mathcal{V}$ and $q \in \mathcal{S}$:

$$\left.\begin{aligned}\int_{{}^{n}\Omega} \Big\{ \mathcal{D}\left(\boldsymbol{w}\right) : 2\left[1 - {}^{n}D\right]\eta\left({}^{n+1}_{(m+1)}\boldsymbol{v}\right)\mathcal{D}\left({}^{n+1}_{(m+1)}\boldsymbol{v}\right) \\ - \left[1 - {}^{n}D\right]\left[\nabla\cdot\boldsymbol{w}\right]\left[{}^{n+1}_{(m+1)}\widetilde{p}\right] - \psi\left({}^{n}D\right)\boldsymbol{w}\cdot{}^{n}\boldsymbol{b}\Big\}\mathrm{d}\Omega = 0, \\ \\ \int_{{}^{n}\Omega} \psi\left({}^{n}D\right) q\left[\nabla\cdot{}^{n+1}_{(m+1)}\boldsymbol{v}\right]\ \mathrm{d}\Omega = 0,\end{aligned}\right\} \tag{22}$$

where $\boldsymbol{w}$ is a test function for an appropriate vector space $\mathcal{V}$, and q is a test function for an appropriate scalar space $\mathcal{S}$. Using Equations (15-21), The Newton linearization of the above equation can thus be defined as:

Find ${}^{n+1}\delta\boldsymbol{v} \in \mathcal{V}$ and ${}^{n+1}\delta\widetilde{p} \in \mathcal{S}$ such that $\forall\ \boldsymbol{w} \in \mathcal{V}$ and $q \in \mathcal{S}$:

$$\left.\begin{aligned}\int_{{}^{n}\Omega} \mathcal{D}\left(\boldsymbol{w}\right) : \Big\{2\left[1 - {}^{n}D\right]\eta\left({}^{n+1}_{(m)}\boldsymbol{v}\right)\mathcal{D}\left({}^{n+1}\delta\boldsymbol{v}\right)\Big\}\ \mathrm{d}\Omega \\ + \int_{{}^{n}\Omega} \mathcal{D}\left(\boldsymbol{w}\right) : \Big\{2\left[1 - {}^{n}D\right]\eta\left({}^{n+1}_{(m)}\boldsymbol{v}\right)\mathcal{D}\left({}^{n+1}_{(m)}\boldsymbol{v}\right)\Big\}\ \mathrm{d}\Omega \\ + \int_{{}^{n}\Omega} \mathcal{D}\left(\boldsymbol{w}\right) : \{2\left[1 - {}^{n}D\right]\frac{\partial\eta}{\partial\mathcal{D}_{\mathrm{II}}\left({}^{n+1}_{(m)}\boldsymbol{v}\right)}[\mathcal{D}\left({}^{n+1}_{(m)}\boldsymbol{v}\right) : \\ \mathcal{D}\left({}^{n+1}\delta\boldsymbol{v}\right)]\mathcal{D}\left({}^{n+1}_{(m)}\boldsymbol{v}\right)\}\ \mathrm{d}\Omega \\ - \int_{{}^{n}\Omega} \left[1 - {}^{n}D\right]\nabla\cdot\boldsymbol{w}\ \left[{}^{n+1}\delta\widetilde{p} - {}^{n+1}_{(m)}\widetilde{p}\right]\ \mathrm{d}\Omega \\ - \int_{{}^{n}\Omega} \psi\left({}^{n}D\right)\boldsymbol{w}\cdot{}^{n}\boldsymbol{b}\ \mathrm{d}\Omega - \int_{{}^{n}\Gamma^{\mathrm{N}}} \boldsymbol{w}\cdot{}^{n}\bar{\boldsymbol{T}}\ \mathrm{d}\Gamma = 0, \\ \\ \int_{{}^{n}\Omega} \psi\left({}^{n}D\right) q\nabla\cdot\left[{}^{n+1}\delta\boldsymbol{v} + {}^{n+1}_{(m)}\boldsymbol{v}\right]\ \mathrm{d}\Omega = 0,\end{aligned}\right\} \text{ on } {}^{n}\Omega, \tag{23}$$

The algorithmic implementation is provided below in Algorithm 1. To verify the Newton's method, we repeat the study from Section 4.1 in the main article wherein show that the nonlinear Stokes formulation converges to the manufactured solution presented in [14, 15] for incompressible flow. This solution is given by

$$\begin{aligned} v_1^* &= x_1 + x_1^2 - 2x_1x_2 + x_1^3 - 3x_1x_2^2 + x_1^2x_2, \\ v_2^* &= -x_2 - 2x_1x_2 + x_2^2 - 3x_1^2x_2 + x_2^3 - x_1x_2^2, \\ p^* &= x_1x_2 + x_1 + x_2 + x_1^3x_2^2 - 4/3. \end{aligned} \tag{24}$$

For this study we employ P2-P1 (Taylor-Hood) elements and take the viscosity parameter $N = 3.5$, as was done in Section 4.1. Starting with a 4×4 structured

Table 2: Numerical verification study of the nonlinear Stokes model using Newton iteration scheme. The L^2 error norms $\varepsilon_{\boldsymbol{v}}$ and ε_p for velocity magnitude and pressure, respectively, given in Equations (25) are presented for different mesh sizes.

Mesh	**#DoF**	$\varepsilon_{\boldsymbol{v}}$	**Rate**	ε_p	**Rate**
4×4	187	$5.36\text{e}-4$	$--$	$9.74\text{e}-2$	$--$
8×8	659	$5.00\text{e}-5$	3.42	$1.54\text{e}-2$	2.66
16×16	2467	$3.64\text{e}-6$	3.78	$1.95\text{e}-3$	2.98
32×32	9539	$2.36\text{e}-7$	3.95	$2.67\text{e}-4$	2.87

mesh over the unit domain Ω, we progressively refine the mesh by reducing the element size by half. For each mesh size we compute the L^2 error norms,

$$\varepsilon_{\boldsymbol{v}} = \sqrt{\frac{\sum_{k=1}^{\mathrm{N^{P2}}} \left(||\boldsymbol{v}||_k - ||\boldsymbol{v}^*||_k\right)^2}{\sum_{k=1}^{\mathrm{N^{P2}}} \left(||\boldsymbol{v}^*||_k\right)^2}}, \quad \varepsilon_p = \sqrt{\frac{\sum_{k=1}^{\mathrm{N^{P1}}} \left(p_k - p_k^*\right)^2}{\sum_{k=1}^{\mathrm{N^{P1}}} \left(p_k^*\right)^2}}, \tag{25}$$

for velocity magnitude and pressure, respectively, which are reported in Table 2. In the above equations, $\mathrm{N^{P1}}$ and $\mathrm{N^{P2}}$ are the number of nodes in the P2 and P1 spaces, respectively; and $||\boldsymbol{v}||_k$ and p_k are the velocity magnitude and pressure, respectively, at the k-th node. The $\varepsilon_{\boldsymbol{v}}$ and ε_p error norms and rates of convergence with respect to mesh size are nearly identical to those reported in Section 4.1 of the main article (i.e., when using the Picard iteration scheme), thus verifying the approach. The Newton's method also required far fewer iterations than the Picard iteration scheme to converge to the solution within the same error tolerance, as detailed in Table 3. From this verification study we conclude that the Newton's method is computationally more efficient than the Picard iteration scheme under ideal conditions (e.g., a convex domain). However, upon the introduction of a notch or a damage zone in the domain, we found that the Newton's method when implemented in FEniCS is not guaranteed to converge, whereas the Picard iteration scheme never fails to converge. We suspect the issue with the Newton's method arises due to either interpolation errors during the automated assembly of the system tangent in FEniCS, or, due to the choice of the regularization parameter γ incorporated to avoid zero-viscosity when assuming zero or constant velocity initial guess for the Stokes equations. We expect to investigate this further as we begin to simulate crevasse propagation in 3D using parallel computing and scalable algorithms.

Algorithm 1 : Newton iteration scheme for Stokes flow in 2D

Let ${}^{n+1}_{(m)}\boldsymbol{v}$ denote the velocity vector with horizontal components ${}^{n+1}_{(m)}v_1$ and ${}^{n+1}_{(m)}v_2$, respectively, and ${}^{n+1}_{(m)}\widetilde{p}$ denote the effective pressure determined on the updated reference configuration ${}^{n+1}\Omega$ at Newton iteration m. Likewise let ${}^{n+1}\delta\boldsymbol{v}$ and ${}^{n+1}\delta\widetilde{p}$ denote the velocity and effective pressure increments, respectively, between Newton iterations m and $m+1$ as presented in Equation (16).

1. Initialize at $m = 0$ by setting ${}^{n+1}_{(0)}\boldsymbol{v} = {}^{n}\boldsymbol{v}$ and ${}^{n+1}_{(0)}\widetilde{p} = {}^{n}\widetilde{p}$ everywhere in the domain.
2. Initialize the maximum relative error ε to be greater than the chosen tolerance ε_{tol}.
3. While $\varepsilon > \varepsilon_{\text{tol}}$:
   (a) Solve the Stokes equations (Eq. 23) to obtain the viscosity and pressure increments, ${}^{n+1}\delta\boldsymbol{v}$ and ${}^{n+1}\delta\widetilde{p}$, respectively. This is done in FEniCS software using the `solve()` function.
   (b) Obtain the updated solutions for velocity and pressure: ${}^{n+1}_{(m+1)}\boldsymbol{v} = {}^{n+1}\delta\boldsymbol{v} + {}^{n+1}_{(m)}\boldsymbol{v}$ and ${}^{n+1}_{(m+1)}\widetilde{p} = {}^{n+1}\delta\widetilde{p} + {}^{n+1}_{(m)}\widetilde{p}$.
   (c) Calculate relative L^2 error norms: $\varepsilon_1 = \frac{||{}^{n+1}\delta v_1||}{||{}^{n+1}_{(m+1)}v_1||}$, $\varepsilon_2 = \frac{||{}^{n+1}\delta v_2||}{||{}^{n+1}_{(m+1)}v_2||}$, $\varepsilon_p = \frac{||{}^{n+1}\delta\widetilde{p}||}{||{}^{n+1}_{(m+1)}\widetilde{p}||}$.
   (d) Determine the maximum relative error: $\varepsilon = \max\{\varepsilon_1, \varepsilon_2, \varepsilon_p\}$.
   (e) Update the iteration count: $m = m + 1$.
4. Upon convergence: ${}^{n+1}v_1 = {}^{n+1}_{(m+1)}v_1$, ${}^{n+1}v_2 = {}^{n+1}_{(m+1)}v_2$, and ${}^{n+1}\widetilde{p} = {}^{n+1}_{(m+1)}\widetilde{p}$.

Table 3: Number of iterations required to converge within the error tolerance $\varepsilon_{\mathrm{tol}} = 10^{-8}$ for the Picard iteration scheme and the Newton's method. The asymptotic convergence of the Newton's method is evident from the relatively few iterations required for convergence as compared to the Picard iteration scheme.

Mesh	**Picard Iterations**	**Newton Iterations**
4×4	45	6
8×8	24	5
16×16	26	5
32×32	26	5

References

[1] R. Duddu, H. Waisman, A temperature dependent creep damage model for polycrystalline ice, Mechanics of Materials 46 (2012) 23 – 41.

[2] T. J. Hughes, L. P. Franca, A new finite element formulation for computational fluid dynamics: Vii. the stokes problem with various well-posed boundary conditions: Symmetric formulations that converge for all velocity/pressure spaces, Computer Methods in Applied Mechanics and Engineering 65 (1) (1987) 85 – 96.

[3] L. P. Franca, R. Stenberg, Error analysis of galerkin least squares methods for the elasticity equations, SIAM Journal on Numerical Analysis 28 (6) (1991) 1680–1697.

[4] M. Gunzburger, R. Nicolaides, Incompressible Computational Fluid Dynamics, Cambridge University Press, 1993.

[5] R. Duddu, H. Waisman, A nonlocal continuum damage mechanics approach to simulation of creep fracture in ice sheets, Computational Mechanics 51 (6) (2013) 961–974.

[6] J. Betten, Applications of tensor functions to the formulation of constitutive equations involving damage and initial anisotropy, Engineering Fracture Mechanics 25 (5) (1986) 573 – 584.

[7] D. G. Karr, K. Choi, A three-dimensional constitutive damage model for polycrystalline ice, Mechanics of Materials 8 (1) (1989) 55 – 66.

[8] J. W. Glen, The creep of polycrystalline ice, Proceedings of the Royal Society of London A: Mathematical, Physical and Engineering Sciences 228 (1175) (1955) 519–538.

[9] D. N. Arnold, F. Brezzi, M. Fortin, A stable finite element for the stokes equations, CALCOLO 21 (4) (1984) 337–344.

[10] F. Brezzi, J. Pitkaranta, On the stabilization of finite element approximations of the Stokes equations, Notes on Numerical Fluid Mechanics, Vol. 10, 1984.

[11] T. J. Hughes, J. R. Stewart, A space-time formulation for multiscale phenomena, Journal of Computational and Applied Mathematics 74 (1) (1996) 217 – 229. doi:http://dx.doi.org/10.1016/0377-0427(96)00025-8.
URL http://www.sciencedirect.com/science/article/pii/0377042796000258

[12] D. Z. Turner, K. B. Nakshatrala, K. D. Hjelmstad, On the stability of bubble functions and a stabilized mixed finite element formulation for the stokes problem, International Journal for Numerical Methods in Fluids 60 (12) (2009) 1291–1314.

[13] T. Isaac, G. Stadler, O. Ghattas, Solution of nonlinear stokes equations discretized by high-order finite elements on nonconforming and anisotropic meshes, with application to ice sheet dynamics, SIAM Journal on Scientific Computing 37 (6) (2015) B804–B833. doi:10.1137/140974407.
URL http://dx.doi.org/10.1137/140974407

[14] C. R. Dohrmann, P. B. Bochev, A stabilized finite element method for the stokes problem based on polynomial pressure projections, International Journal for Numerical Methods in Fluids 46 (2004) 183–201. doi:10.1002/fld.752.

[15] J. Worthen, G. Stadler, N. Petra, M. Gurnis, O. Ghattas, Towards adjoint-based inversion for rheological parameters in nonlinear viscous mantle flow, Physics of the Earth and Planetary Interiors 234 (2014) 23 – 34.